Global polarization of Λ hyperons in Au + Au collisions at $\sqrt{s_{NN}} = 200$ GeV

J. Adam,[9] L. Adamczyk,[1] J. R. Adams,[31] J. K. Adkins,[21] G. Agakishiev,[19] M. M. Aggarwal,[33] Z. Ahammed,[56] N. N. Ajitanand,[44] I. Alekseev,[17,28] D. M. Anderson,[46] R. Aoyama,[50] A. Aparin,[19] D. Arkhipkin,[3] E. C. Aschenauer,[3] M. U. Ashraf,[49] F. Atetalla,[20] A. Attri,[33] G. S. Averichev,[19] X. Bai,[7] V. Bairathi,[29] K. Barish,[52] A. J. Bassill,[52] A. Behera,[44] R. Bellwied,[48] A. Bhasin,[18] A. K. Bhati,[33] J. Bielcik,[10] J. Bielcikova,[11] L. C. Bland,[3] I. G. Bordyuzhin,[17] J. D. Brandenburg,[38] A. V. Brandin,[28] D. Brown,[25] J. Bryslawskyj,[52] I. Bunzarov,[19] J. Butterworth,[38] H. Caines,[59] M. Calderón de la Barca Sánchez,[5] J. M. Campbell,[31] D. Cebra,[5] I. Chakaberia,[3,20,42] P. Chaloupka,[10] F.-H. Chang,[30] Z. Chang,[3] N. Chankova-Bunzarova,[19] A. Chatterjee,[56] S. Chattopadhyay,[56] J. H. Chen,[43] X. Chen,[41] X. Chen,[23] J. Cheng,[49] M. Cherney,[9] W. Christie,[3] G. Contin,[24] H. J. Crawford,[4] S. Das,[7] T. G. Dedovich,[19] I. M. Deppner,[53] A. A. Derevschikov,[35] L. Didenko,[3] C. Dilks,[34] X. Dong,[24] J. L. Drachenberg,[22] J. C. Dunlop,[3] L. G. Efimov,[19] N. Elsey,[58] J. Engelage,[4] G. Eppley,[38] R. Esha,[6] S. Esumi,[50] O. Evdokimov,[8] J. Ewigleben,[25] O. Eyser,[3] R. Fatemi,[21] S. Fazio,[3] P. Federic,[11] P. Federicova,[10] J. Fedorisin,[19] P. Filip,[19] E. Finch,[51] Y. Fisyak,[3] C. E. Flores,[5] L. Fulek,[1] C. A. Gagliardi,[46] T. Galatyuk,[12] F. Geurts,[38] A. Gibson,[55] D. Grosnick,[55] D. S. Gunarathne,[45] Y. Guo,[20] A. Gupta,[18] W. Guryn,[3] A. I. Hamad,[20] A. Hamed,[46] A. Harlenderova,[10] J. W. Harris,[59] L. He,[36] S. Heppelmann,[34] S. Heppelmann,[5] N. Herrmann,[53] A. Hirsch,[36] L. Holub,[10] S. Horvat,[59] X. Huang,[49] B. Huang,[8] S. L. Huang,[44] H. Z. Huang,[6] T. Huang,[30] T. J. Humanic,[31] P. Huo,[44] G. Igo,[6] W. W. Jacobs,[16] A. Jentsch,[47] J. Jia,[3,44] K. Jiang,[41] S. Jowzaee,[58] E. G. Judd,[4] S. Kabana,[20] D. Kalinkin,[16] K. Kang,[49] D. Kapukchyan,[52] K. Kauder,[58] H. W. Ke,[3] D. Keane,[20] A. Kechechyan,[19] D. P. Kikoła,[57] C. Kim,[52] T. A. Kinghorn,[5] I. Kisel,[13] A. Kisiel,[57] L. Kochenda,[28] L. K. Kosarzewski,[57] A. F. Kraishan,[45] L. Kramarik,[10] L. Krauth,[52] P. Kravtsov,[28] K. Krueger,[2] N. Kulathunga,[48] S. Kumar,[33] L. Kumar,[33] J. Kvapil,[10] J. H. Kwasizur,[16] R. Lacey,[44] J. M. Landgraf,[3] J. Lauret,[3] A. Lebedev,[3] R. Lednicky,[19] J. H. Lee,[3] X. Li,[41] C. Li,[41] W. Li,[43] Y. Li,[49] Y. Liang,[20] J. Lidrych,[10] T. Lin,[46] A. Lipiec,[57] M. A. Lisa,[31] F. Liu,[7] P. Liu,[44] H. Liu,[16] Y. Liu,[46] T. Ljubicic,[3] W. J. Llope,[58] M. Lomnitz,[24] R. S. Longacre,[3] X. Luo,[7] S. Luo,[8] G. L. Ma,[43] Y. G. Ma,[43] L. Ma,[14] R. Ma,[3] N. Magdy,[44] R. Majka,[59] D. Mallick,[29] S. Margetis,[20] C. Markert,[47] H. S. Matis,[24] O. Matonoha,[10] D. Mayes,[52] J. A. Mazer,[39] K. Meehan,[5] J. C. Mei,[42] N. G. Minaev,[35] S. Mioduszewski,[46] D. Mishra,[29] B. Mohanty,[29] M. M. Mondal,[15] I. Mooney,[58] D. A. Morozov,[35] Md. Nasim,[6] J. D. Negrete,[52] J. M. Nelson,[4] D. B. Nemes,[59] M. Nie,[43] G. Nigmatkulov,[28] T. Niida,[58] L. V. Nogach,[35] T. Nonaka,[50] S. B. Nurushev,[35] G. Odyniec,[24] A. Ogawa,[3] K. Oh,[37] S. Oh,[59] V. A. Okorokov,[28] D. Olvitt, Jr.,[45] B. S. Page,[3] R. Pak,[3] Y. Panebratsev,[19] B. Pawlik,[32] H. Pei,[7] C. Perkins,[4] J. Pluta,[57] J. Porter,[24] M. Posik,[45] N. K. Pruthi,[33] M. Przybycien,[1] J. Putschke,[58] A. Quintero,[45] S. K. Radhakrishnan,[24] S. Ramachandran,[21] R. L. Ray,[47] R. Reed,[25] H. G. Ritter,[24] J. B. Roberts,[38] O. V. Rogachevskiy,[19] J. L. Romero,[5] L. Ruan,[3] J. Rusnak,[11] O. Rusnakova,[10] N. R. Sahoo,[46] P. K. Sahu,[15] S. Salur,[39] J. Sandweiss,[59] J. Schambach,[47] A. M. Schmah,[24] W. B. Schmidke,[3] N. Schmitz,[26] B. R. Schweid,[44] F. Seck,[12] J. Seger,[9] M. Sergeeva,[6] R. Seto,[52] P. Seyboth,[26] N. Shah,[43] E. Shahaliev,[19] P. V. Shanmuganathan,[25] M. Shao,[41] W. Q. Shen,[43] F. Shen,[42] S. S. Shi,[7] Q. Y. Shou,[43] E. P. Sichtermann,[24] S. Siejka,[57] R. Sikora,[1] M. Simko,[11] S. Singha,[20] N. Smirnov,[59] D. Smirnov,[3] W. Solyst,[16] P. Sorensen,[3] H. M. Spinka,[2] B. Srivastava,[36] T. D. S. Stanislaus,[55] D. J. Stewart,[59] M. Strikhanov,[28] B. Stringfellow,[36] A. A. P. Suaide,[40] T. Sugiura,[50] M. Sumbera,[11] B. Summa,[34] Y. Sun,[41] X. Sun,[7] X. M. Sun,[7] B. Surrow,[45] D. N. Svirida,[17] P. Szymanski,[57] Z. Tang,[41] A. H. Tang,[3] A. Taranenko,[28] T. Tarnowsky,[27] J. H. Thomas,[24] A. R. Timmins,[48] D. Tlusty,[38] T. Todoroki,[3] M. Tokarev,[19] C. A. Tomkiel,[25] S. Trentalange,[6] R. E. Tribble,[46] P. Tribedy,[3] S. K. Tripathy,[15] O. D. Tsai,[6] B. Tu,[7] T. Ullrich,[3] D. G. Underwood,[2] I. Upsal,[31] G. Van Buren,[3] J. Vanek,[11] A. N. Vasiliev,[35] I. Vassiliev,[13] F. Videbæk,[3] S. Vokal,[19] S. A. Voloshin,[58] A. Vossen,[16] G. Wang,[6] Y. Wang,[7] F. Wang,[36] Y. Wang,[49] J. C. Webb,[3] L. Wen,[6] G. D. Westfall,[27] H. Wieman,[24] S. W. Wissink,[16] R. Witt,[54] Y. Wu,[20] Z. G. Xiao,[49] G. Xie,[8] W. Xie,[36] Q. H. Xu,[42] Z. Xu,[3] J. Xu,[7] Y. F. Xu,[43] N. Xu,[24] S. Yang,[3] C. Yang,[42] Q. Yang,[42] Y. Yang,[30] Z. Ye,[8] Z. Ye,[8] L. Yi,[42] K. Yip,[3] I.-K. Yoo,[37] N. Yu,[7] H. Zbroszczyk,[57] W. Zha,[41] Z. Zhang,[43] L. Zhang,[7] Y. Zhang,[41] X. P. Zhang,[49] J. Zhang,[23] S. Zhang,[43] S. Zhang,[41] J. Zhang,[24] J. Zhao,[36] C. Zhong,[43] C. Zhou,[43] L. Zhou,[41] Z. Zhu,[42] X. Zhu,[49] and M. Zyzak[13]

(STAR Collaboration)

[1]*AGH University of Science and Technology, FPACS, Cracow 30-059, Poland*

[2]*Argonne National Laboratory, Argonne, Illinois 60439*

[3]*Brookhaven National Laboratory, Upton, New York 11973*

[4]*University of California, Berkeley, California 94720*

[5]*University of California, Davis, California 95616*

[6]*University of California, Los Angeles, California 90095*

[7]*Central China Normal University, Wuhan, Hubei 430079*

[8]*University of Illinois at Chicago, Chicago, Illinois 60607*

[9]*Creighton University, Omaha, Nebraska 68178*

[10]*Czech Technical University in Prague, FNSPE, Prague, 115 19, Czech Republic*

[11]*Nuclear Physics Institute AS CR, Prague 250 68, Czech Republic*

[12]*Technische Universitat Darmstadt, Darmstadt 64289, Germany*

[13]*Frankfurt Institute for Advanced Studies FIAS, Frankfurt 60438, Germany*

 ©2018 American Physical Society

[14]*Fudan University, Shanghai, 200433*
[15]*Institute of Physics, Bhubaneswar 751005, India*
[16]*Indiana University, Bloomington, Indiana 47408*
[17]*Alikhanov Institute for Theoretical and Experimental Physics, Moscow 117218, Russia*
[18]*University of Jammu, Jammu 180001, India*
[19]*Joint Institute for Nuclear Research, Dubna, 141 980, Russia*
[20]*Kent State University, Kent, Ohio 44242*
[21]*University of Kentucky, Lexington, Kentucky 40506-0055*
[22]*Lamar University, Physics Department, Beaumont, Texas 77710*
[23]*Institute of Modern Physics, Chinese Academy of Sciences, Lanzhou, Gansu 730000*
[24]*Lawrence Berkeley National Laboratory, Berkeley, California 94720*
[25]*Lehigh University, Bethlehem, Pennsylvania 18015*
[26]*Max-Planck-Institut fur Physik, Munich 80805, Germany*
[27]*Michigan State University, East Lansing, Michigan 48824*
[28]*National Research Nuclear University MEPhI, Moscow 115409, Russia*
[29]*National Institute of Science Education and Research, HBNI, Jatni 752050, India*
[30]*National Cheng Kung University, Tainan 70101*
[31]*Ohio State University, Columbus, Ohio 43210*
[32]*Institute of Nuclear Physics PAN, Cracow 31-342, Poland*
[33]*Panjab University, Chandigarh 160014, India*
[34]*Pennsylvania State University, University Park, Pennsylvania 16802*
[35]*Institute of High Energy Physics, Protvino 142281, Russia*
[36]*Purdue University, West Lafayette, Indiana 47907*
[37]*Pusan National University, Pusan 46241, Korea*
[38]*Rice University, Houston, Texas 77251*
[39]*Rutgers University, Piscataway, New Jersey 08854*
[40]*Universidade de Sao Paulo, Sao Paulo, 05314-970, Brazil*
[41]*University of Science and Technology of China, Hefei, Anhui 230026*
[42]*Shandong University, Jinan, Shandong 250100*
[43]*Shanghai Institute of Applied Physics, Chinese Academy of Sciences, Shanghai 201800*
[44]*State University of New York, Stony Brook, New York 11794*
[45]*Temple University, Philadelphia, Pennsylvania 19122*
[46]*Texas A&M University, College Station, Texas 77843*
[47]*University of Texas, Austin, Texas 78712*
[48]*University of Houston, Houston, Texas 77204*
[49]*Tsinghua University, Beijing 100084*
[50]*University of Tsukuba, Tsukuba, Ibaraki 305-8571, Japan*
[51]*Southern Connecticut State University, New Haven, Connecticut 06515*
[52]*University of California, Riverside, California 92521*
[53]*University of Heidelberg, Heidelberg 69120, Germany*
[54]*United States Naval Academy, Annapolis, Maryland 21402*
[55]*Valparaiso University, Valparaiso, Indiana 46383*
[56]*Variable Energy Cyclotron Centre, Kolkata 700064, India*
[57]*Warsaw University of Technology, Warsaw 00-661, Poland*
[58]*Wayne State University, Detroit, Michigan 48201*
[59]*Yale University, New Haven, Connecticut 06520*

(Received 13 May 2018; published 23 July 2018)

Global polarization of Λ hyperons has been measured to be of the order of a few tenths of a percentage in Au+Au collisions at $\sqrt{s_{NN}} = 200$ GeV, with no significant difference between Λ and $\bar{\Lambda}$. These new results reveal the collision energy dependence of the global polarization together with the results previously observed at $\sqrt{s_{NN}} = 7.7$–62.4 GeV and indicate noticeable vorticity of the medium created in noncentral heavy-ion collisions at the highest Relativistic Heavy Ion Collider collision energy. The signal is in rough quantitative agreement with the theoretical predictions from a hydrodynamic model and from a multi-phase transport model. The polarization is larger in more peripheral collisions, and depends weakly on the hyperon's transverse momentum and pseudorapidity η^H within $|\eta^H| < 1$. An indication of the polarization dependence on the event-by-event

charge asymmetry is observed at the 2σ level, suggesting a possible contribution to the polarization from the axial current induced by the initial magnetic field.

DOI: 10.1103/PhysRevC.98.014910

I. INTRODUCTION

Nucleus-nucleus collisions at the Relativistic Heavy Ion Collider (RHIC) and at the Large Hadron Collider produce a state of partonic matter, the quark-gluon plasma (QGP), that is expected to have existed in nature right after the Big Bang [1]. Various experimental observations together with sophisticated theoretical calculations indicate that the QGP behaves as a nearly perfect liquid, i.e., a fluid with the lowest ratio of shear viscosity to entropy density (η/s) [2–4].

One of the most important observables in heavy-ion experiments is the azimuthal anisotropic flow that is usually quantified by the Fourier coefficients of the azimuthal distribution of the final-state particles relative to the collision symmetry planes. The first-order coefficient, called the directed flow, is argued to be sensitive to the equation of state of the matter and could serve as a possible signature of the QGP phase transition [5–7]. The second-order coefficient, elliptic flow, offers strong evidence for the fluidlike behavior of the created matter. Furthermore, the higher-order coefficients are found to provide additional constraints on η/s and the initial conditions. In spite of a successful description of the flow observables for $n \geqslant 2$ by hydrodynamic models, none of the theoretical models can describe quantitatively the directed flow. This indicates that the current models still lack an important ingredient in the description of relativistic heavy-ion collision dynamics. The initial condition in the longitudinal direction would play an important role for the directed flow and vorticity [8,9].

Several theoretical models suggest that the large angular momentum carried by two colliding nuclei [10–12] can be transferred to the created system. As a consequence, the spin of particles composing the system might be globally polarized along the direction of the system angular momentum, due to spin-orbit coupling. Such a global polarization can be measured experimentally with hyperons via parity-violating weak decays, in which the daughter baryon is preferentially emitted in the direction of the hyperon spin. If the parent hyperon is an antiparticle, then the daughter baryon tends to be emitted in the opposite direction to the parent spin.

The angular distribution of daughter baryons in the hyperon decays is given by

$$\frac{dN}{d\cos\theta^*} \propto 1 + \alpha_H P_H \cos\theta^*, \tag{1}$$

where α_H is the hyperon decay constant, P_H is the hyperon polarization, and θ^* is the angle between the momentum of daughter baryon and the polarization vector in the hyperon rest frame. Since the angular momentum of the system is perpendicular to the reaction plane (a plane defined by the impact parameter vector and the beam direction), the polarization of hyperons can be measured via the azimuthal distribution of daughter baryons with respect to the reaction plane in the hyperon rest frame, similarly to anisotropic flow measurements [3].

The STAR Collaboration performed the first global polarization measurements of Λ hyperons in Au+Au collisions at $\sqrt{s_{NN}} = 62.4$ and 200 GeV in 2007 [13]. These results were consistent with zero within large statistical uncertainties. More recently, the STAR Collaboration has reported a nonzero signal for the Λ global polarization in Au+Au collisions at lower energies ($\sqrt{s_{NN}} = 7.7$–39 GeV) [14], with a possible difference between Λ and $\bar{\Lambda}$ polarizations that may indicate the effect of the spin alignment by the initial magnetic field. These results can be qualitatively described by hydrodynamic and transport models [15,16]. The global polarization seems to decrease with increasing collision energy, and those models predict a finite signal ($\sim$0.2%) at the top RHIC energy, $\sqrt{s_{NN}} = 200$ GeV. It is thus important to measure the global polarization signal at $\sqrt{s_{NN}} = 200$ GeV with all available statistics in order to enhance understanding of the role of vorticity in heavy-ion collisions. It is likely related to other observables such as directed flow, elliptic flow, and the source tilt of the system measured via femtoscopy [9,12,17]. Reference [18] explains the observed global polarization as a result of the axial charge separation due to the chiral vortical effect. Similarly to the chiral magnetic effect, which is the induction of an electric current along the magnetic field in a medium with nonzero axial charge, an axial current can be generated in the medium with nonzero baryon chemical potential by the system vorticity via the chiral vortical effect (for a recent review of the chiral anomalous effects in heavy-ion collisions, see Ref. [19]). Thus the global polarization measurements might provide important information on the chiral dynamics of the system. Furthermore, precise measurements of the difference in the polarization between Λ and $\bar{\Lambda}$ provide constraints on the magnitude and the lifetime of the magnetic field in heavy-ion collisions [20].

In this paper, we present results of the global polarization of Λ and $\bar{\Lambda}$ hyperons in Au+Au collisions at $\sqrt{s_{NN}} = 200$ GeV using the data recorded by the STAR experiment in the years 2010, 2011, and 2014. The total data set is about 150 times larger than the data set analyzed in the previous search by STAR for hyperon polarization in Au+Au collisions at $\sqrt{s_{NN}} = 200$ GeV [13]. We present the results as functions of the collision centrality, the hyperon's transverse momentum, and pseudorapidity. We also present comparisons with available theoretical calculations. Furthermore, we present the dependence of the polarization on the event-by-event charge asymmetry to study a possible relation between the polarization and axial current induced by the initial magnetic field [21].

II. STAR EXPERIMENT

The STAR detector is composed of central barrel detectors used for tracking and particle identification, and trigger detectors located in the forward and backward directions [22]. Charged tracks were measured using the time projection chamber (TPC) [23], which covers the full azimuth and a

pseudorapidity range of $-1 < \eta < 1$. Momenta of charged particles were determined via trajectories of reconstructed tracks and a primary vertex was reconstructed by extrapolating the tracks back to the origin. The TPC also allows particle identification based on the ionization energy loss, dE/dx, in the TPC gas (Ar 90% + CH_4 10%).

The time-of-flight detector (TOF) [24] is installed outside the TPC, covering the full azimuth and a pseudorapidity range of $-0.9 < \eta < 0.9$. Multigap resistive plate chamber (MRPC) technology is employed for the STAR TOF detector. The TOF system consists of 120 trays and each tray has 32 MRPCs. The timing resolution of the TOF system with a start time from the vertex position detectors (VPD) [25] is ~100 ps. The TOF extends the capability of particle identification provided by the TPC up to $p_T = 3\,\mathrm{GeV}/c$.

The zero degree calorimeters (ZDC) [26] and the VPD were used to determine a minimum-bias trigger. The ZDCs are located at forward (west) and backward (east) angles, $|\eta| > 6.3$. The ZDCs are Cherenkov-light sampling calorimeters and each ZDC is composed of three identical modules. They measure the energy deposit of spectator neutrons. The VPD consists of two identical sets of detectors located at forward and backward rapidities and surrounds the beam pipe, covering a pseudorapidity range of $4.24 < |\eta| < 5.1$. Each VPD consists of nineteen modules, which is composed of a plastic scintillator with a Pb converter. The VPD also provides the start time of collisions and the position of the collision vertex along the beam direction.

III. DATA ANALYSIS

The analysis is based on the data for Au+Au collisions at $\sqrt{s_{NN}} = 200$ GeV taken in the years 2010, 2011, and 2014 with a minimum-bias trigger selected by a coincidence signal between the east and west VPDs. The collision vertex along the beam direction was required to be within 30 cm of the center of the TPC for 2010 and 2011 data and to be within 6 cm for 2014 data. In the 2014 data the narrower vertex selection was required to ensure a good acceptance for the Heavy Flavor Tracker (HFT) installed prior to 2014 run [27,28] (Note that the HFT was not used in this analysis). Additionally, the difference between the vertex positions along the beam direction determined by the TPC and the VPD was required to be less than 3 cm to reduce the beam-induced background. The vertex position in the transverse plane was limited to be within 2 cm from the beam line. These selection criteria yielded 200 million events using the 2010 data set, 350 million events using the 2011 data set, and one billion events using the 2014 data set. The collision centrality was determined based on the measured multiplicity of charged tracks within $|\eta| < 0.5$, and this was matched to a Monte Carlo Glauber simulation in the same way as in previous studies [29]. The effect of the trigger efficiency was taken into account in the analysis by weighting events especially in peripheral collisions when calculating final results, although the effect is very small.

A. Event plane determination

As an experimental estimate of the reaction plane, the first-order event plane Ψ_1 was determined by the ZDCs that are equipped with Shower Maximum Detectors (SMD) [26,30,31]. The ZDCs measure the energy deposited by spectator neutrons, and the SMDs measure the centroid of the hadronic shower caused by the interaction between spectator neutrons and the ZDC. Since the spectator neutrons are deflected outward from the centerline of the collisions [32], we can determine the direction of the angular momentum of the system (see Ref. [33] for more details). The event plane resolution, $\mathrm{Res}(\Psi_1) = \langle \cos(\Psi_1 - \Psi_1^{\mathrm{obs}}) \rangle$, was estimated by the two-subevent method [34], where Ψ_1^{obs} denotes a measured event plane. Figure 1 shows the event plane resolution for the year 2011 data as an example. The resolution reaches a maximum of ~0.39 around 30–40% centrality for the combined plane of ZDC-SMD east and west. The resolution is consistent between 2010 and 2011 data and is better by ~5% for 2014 data compared to that for 2011.

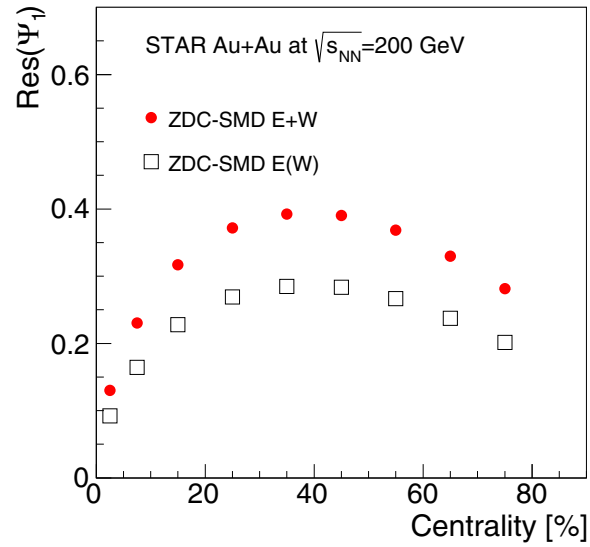

FIG. 1. Resolution of the first-order event plane determined by the ZDC-SMDs [26] in Au+Au collisions at $\sqrt{s_{NN}} = 200$ GeV; ZDC-SMD E+W denotes the combined plane of ZDC-SMDs in east and west sides and ZDC-SMD E(W) denotes one of the ZDC-SMDs.

B. Track selection

Charged tracks reconstructed from the TPC hit information were selected with the following requirements to assure good quality. The number of hit points used in the reconstruction was required to be greater than 14. The ratio of the number of hit points used to the maximum possible number of hit points (45 for a track traversing the entire TPC, but the maximum number can be smaller when track trajectory reaches an endcap of the TPC) was required to be larger than 0.52. Tracks corresponding to $0.15 < p_T < 10\ \mathrm{GeV}/c$ and $|\eta| < 1$ were used in this study.

C. Λ reconstruction

Λ hyperons were identified via decay channels $\Lambda \to p + \pi^-$ and $\bar{\Lambda} \to \bar{p} + \pi^+$. These decay modes account for $(63.9 \pm 0.5)\%$ of all decays [35]. The daughter particles of Λ and $\bar{\Lambda}$, i.e., charged pions and protons, were identified by using dE/dx information from the TPC and time-of-flight information from

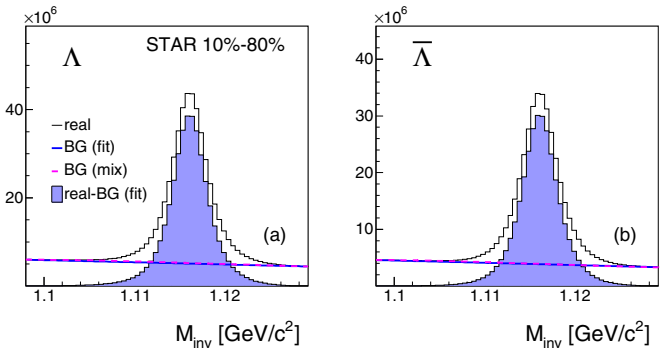

FIG. 2. Invariant mass distributions of the $(p,\ \pi^-)$ system for Λ (a) and of the $(\bar{p},\ \pi^+)$ system for $\bar{\Lambda}$ (b) in the 30–40% centrality bin for 2014 data. Bold solid lines show the background distribution obtained by a linear fitting function, and dashed lines show the background from mixed events. Shaded areas show the extracted signal after the background subtraction using the fitting function.

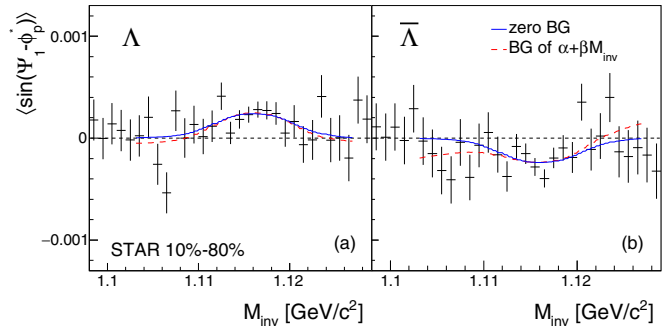

FIG. 3. $\langle\sin(\Psi_1-\phi_p^*)\rangle$ as a function of the invariant mass for Λ (a) and $\bar{\Lambda}$ (b) in the 10–80% centrality bin for 2014 data. Solid and dashed lines show the fitting function for actual fit range, Eq. (3), with two different background assumptions.

the TOF detector, like in our previous publication [33]. Charged pions and protons were selected by requiring the track to be within three standard deviations (3σ) from their peaks in the normalized dE/dx distribution. If the track had TOF hit information, then a constraint based on the square of the measured mass was required. If the TOF information was not available, then an additional cut based on dE/dx was applied, requiring pions (protons) to be 3σ away from the proton (pion) peak in the normalized dE/dx distribution.

The invariant mass, $M_{\rm inv}$, was calculated using candidates for the daughter tracks. To reduce the combinatorial background, selection criteria based on the following decay topology parameters were used:

(i) Distance of the closest approach (DCA) between daughter tracks and the primary vertex,
(ii) DCA between reconstructed trajectories of Λ ($\bar{\Lambda}$) candidates and the primary vertex,
(iii) DCA between two daughter tracks, and
(iv) Decay length of Λ ($\bar{\Lambda}$) candidates.

Furthermore Λ ($\bar{\Lambda}$) candidates were required to point away from the primary vertex. Cuts on the decay topology were adjusted, depending on the collision centrality, to account for the variation of the combinatorial background with centrality. The background level relative to the Λ ($\bar{\Lambda}$) signal in the Λ mass region falls below 30% at maximum in this analysis. Finally, Λ and $\bar{\Lambda}$ with $0.5 < p_T < 6$ GeV/c and $|\eta| < 1$ were analyzed in this study.

Figure 2 shows the invariant mass distributions for Λ and $\bar{\Lambda}$ in the 10–80% centrality bin for 2014 data as an example. The combinatorial background under the Λ peak was estimated by fitting the off-peak region with a linear function, and by the event mixing technique [36], shown in Fig. 2 as solid and dashed lines, respectively.

D. Polarization measurement

As mentioned in Sec. I, the global polarization can be measured via analysis of the azimuthal distribution of daughter protons in the Λ rest frame relative to the reaction plane. As mentioned in Sec. III A, the first-order event plane Ψ_1 determined by the spectator fragments was used in this analysis as an estimator of the reaction plane. The sideward deflection of the spectators allows us to know the direction of the initial angular momentum. Taking into account the experimental resolution of the event plane, the polarization projected onto the direction of the system global angular momentum can be obtained by [13]:

$$P_H = \frac{8}{\pi\alpha_H}\frac{\left\langle \sin\left(\Psi_1^{\rm obs}-\phi_p^*\right)\right\rangle}{\mathrm{Res}(\Psi_1)}, \tag{2}$$

where α_H are the decay parameters of Λ (α_Λ) and $\bar{\Lambda}$ ($\alpha_{\bar{\Lambda}}$), $\alpha_\Lambda = -\alpha_{\bar{\Lambda}} = 0.642 \pm 0.013$ [35]. The angle ϕ_p^* denotes the azimuthal angle of the daughter proton in the Λ rest frame. The $\mathrm{Res}(\Psi_1)$ is the resolution of the first-order event plane. Two different techniques were used to extract the polarization signal $\langle\sin(\Psi_1-\phi_p^*)\rangle$: the invariant mass method and the event plane method, both of which are often used in flow analyses [3,37].

In the invariant mass method [36,37], the mean value of the sine term in Eq. (2) was measured as a function of the invariant mass. Since the Λ particles and background cannot be separated on an event-by-event basis, the observed polarization signal is the sum of the signal and background:

$$\langle\sin(\Psi_1-\phi_p^*)\rangle^{\rm obs} = (1-f^{\rm Bg}(M_{\rm inv}))\langle\sin(\Psi_1-\phi_p^*)\rangle^{\rm Sg} + f^{\rm Bg}(M_{\rm inv})\langle\sin(\Psi_1-\phi_p^*)\rangle^{\rm Bg}, \tag{3}$$

where $f^{\rm Bg}(M_{\rm inv})$ is the background fraction at the invariant mass $M_{\rm inv}$. The term $\langle\sin(\Psi_1-\phi_p^*)\rangle^{\rm Sg}$ is the polarization signal for Λ ($\bar{\Lambda}$), where the term $\langle\sin(\Psi_1-\phi_p^*)\rangle^{\rm Bg}$ is the background contribution, which is in general expected to be zero, but could be nonzero, for example, due to misidentification of particles or errors in track reconstruction. The data were fitted with Eq. (3) to extract the polarization signal. Since the shape of the background as a function of invariant mass is unknown, two assumptions concerning the background contribution were tested: a linear function over $M_{\rm inv}$ ($\langle\sin(\Psi_1-\phi_p^*)\rangle^{\rm Bg} = \alpha + \beta M_{\rm inv}$) and zero background contribution ($\alpha = 0,\ \beta = 0$). Figure 3 shows the observed $\langle\sin(\Psi_1-\phi_p^*)\rangle$ as a function of

the invariant mass $M_{\rm inv}$. Since the daughter proton tends to be emitted in the direction of the parent hyperon spin, and in the opposite direction for antiparticles, the $\langle \sin(\Psi_1 - \phi_p^*)\rangle$ for $\bar{\Lambda}$ shows negative values around its mass region as shown in Fig. 3(b), while it is positive for Λ as in Fig. 3(a). We found that results from these two background assumptions give consistent results within uncertainties, and the difference was incorporated in the systematic uncertainty as described in the following section.

Although the invariant mass method was used as the default method in this analysis, the event plane method was also tested as a systematic check. In the event plane method, the same procedure as used in flow analyses was utilized [3]. First, the number of Λ and $\bar{\Lambda}$ was counted in each bin of the hyperon emission azimuthal angle relative to the event plane after the background subtraction, as demonstrated in Fig. 2. Then the yield of Λ and $\bar{\Lambda}$ as a function of $\Psi_1 - \phi^*$ was fitted with a sine function to obtain the mean sine $\langle \sin(\Psi_1 - \phi_p^*)\rangle^{\rm Sg}$. The difference in results from the invariant mass and event plane methods is included in the systematic uncertainty.

E. Effect of feed-down

A sizable number of Λ and $\bar{\Lambda}$ produced in the collisions are secondary particles—products of heavier particle decays, such as $\Sigma^* \to \Lambda + \pi$, $\Sigma^0 \to \Lambda + \gamma$, and $\Xi \to \Lambda + \pi$. The parent particles are also polarized. The polarization is transferred from the parent particle to the daughter Λ. The contribution of such feed-down to the measured polarization was studied in Refs. [15,16,20] and was found to dilute the polarization of the primary Λ by 15–20%. Note that this estimate is model dependent. In addition, this effect might be smaller in our analysis due to reduction of secondary particles by cuts on the decay topology of Λ. Below, the results are compared to models which do and do not take into account the feed-down effect.

F. Systematic uncertainties

The systematic uncertainties were estimated by varying topological cuts and comparing the results obtained with different methods for the signal extraction and for the event plane determination. Below we describe each systematic source and provide typical values.

We applied 10 different topological cuts and used the standard deviation from the default cut set results as the symmetric systematic uncertainty. The effect from the variation of the topological cuts was found to be $<3\%$.

As described in the previous section, two different techniques were used to extract the polarization signal. We used the result obtained with the invariant mass method as default results, and the difference in the results from the event plane method was included in the systematic uncertainty. The difference in polarization based on different methods was found to be $\sim 21\%$.

The first-order event plane determined by both ZDC-SMDs in the east and west sides was used in this analysis. For a cross-check, the event plane determined by each ZDC-SMD on its own was also used in the analysis, although the poorer event-plane resolution resulted in larger statistical uncertainties. The difference between the results was included in the systematic uncertainty ($\sim 22\%$).

According to Ref. [35], the decay parameter for $\Lambda \to p + \pi^-$, α_Λ, is 0.642 ± 0.013, while $\alpha_{\bar{\Lambda}} = -0.71 \pm 0.08$ for $\bar{\Lambda} \to \bar{p} + \pi^+$, based on world-average data. If charge conjugation and parity symmetry is preserved, $\alpha_\Lambda = -\alpha_{\bar{\Lambda}}$. In this study, we use $\alpha_\Lambda = -\alpha_{\bar{\Lambda}} = 0.642 \pm 0.013$ and the uncertainty in α_H was incorporated into the systematic uncertainty ($\sim 2\%$). Also, the difference from the case using $\alpha_{\bar{\Lambda}} = -0.71$, which we found to be $\sim 9.6\%$, was included in the systematic uncertainty for $\bar{\Lambda}$.

As mentioned in Sec. III C, the combinatorial background in the invariant mass distributions for Λ and $\bar{\Lambda}$ was estimated by a linear function fit and by the event mixing technique as shown in Fig. 2. The difference between the results obtained with the two approaches was included in the systematic uncertainty ($<1\%$).

In the invariant mass method, the background contribution in the off-peak region of Λ ($\bar{\Lambda}$) mass distribution is unknown but is supposed to be zero as mentioned in Sec. III D. We confirmed that the background signal was consistent with zero when increasing the background by applying looser topological cuts. Therefore, the results from the zero-background assumption for the fitting function were used as the final results, and the difference from the nonzero background assumption was included in the systematic uncertainty ($\sim 13\%$).

Final systematic uncertainties were calculated by taking the square root of the quadratic sum of the difference between the default condition and each systematic source. We further examined whether there is a possible experimental bias in our results. The data for Au+Au collisions in the years 2010 and 2011 were taken with two different polarities of the magnetic field. In order to check the effect of the magnetic field configuration, we divided the data into two groups according to the magnetic field polarity and confirmed that there was no significant difference between the two groups. Those two groups also correspond to different times of data taking. Despite changes in the trigger conditions, which had the effect of further improving data taking during runs, and the associated change in the detector conditions, no significant difference in the polarization results was observed.

We also calculated the cumulant terms in a similar way as described in Ref. [38,39] and subtracted them from the observed signal to check for a possible detector effect due to nonuniformity in acceptance and a residual detector effect coming from the event plane calibration:

$$\langle\langle \sin(\Psi_1 - \phi_p^*)\rangle\rangle - \langle\langle \sin\Psi_1\rangle\rangle\langle\langle \cos\phi_p^*\rangle\rangle + \langle\langle \cos\Psi_1\rangle\rangle\langle\langle \sin\phi_p^*\rangle\rangle, \tag{4}$$

where the double angle brackets indicate an average over particles first and then an average over events. It was found that the correction terms are negligible and there was no significant difference in the results beyond the current uncertainty due to the correction. Therefore we did not apply this correction to the final results.

The effect of the tracking efficiency was studied using a Geant simulation [38] and found to be negligible. Also, the acceptance correction proposed in our previous analysis

[13] was applied. The measured polarization can be written as

$$\frac{8}{\pi\alpha_H}\langle\sin(\Psi_{\rm RP}-\phi_p^*)\rangle = A_0\left(p_T^H,\eta^H\right)P_H\left(p_T^H,\eta^H\right), \quad (5)$$

where A_0 is an acceptance correction factor defined as

$$A_0\left(p_T^H,\eta^H\right) = \frac{4}{\pi}\langle\sin\theta_p^*\rangle. \quad (6)$$

The correction factor A_0 was estimated using the experimental data.

The analysis was performed separately for each data set taken in different years. As mentioned in Sec. III A, the event plane resolution slightly differs in each year due to different detector conditions. Also, for the 2014 data, the tracking efficiency became worse at low p_T because of the HFT. We confirmed that this additional inefficiency does not affect our final results. Since the results from the years 2010, 2011, and 2014 were consistent within their uncertainties, we combined all results for the measured P_H to improve the statistical significance.

IV. RESULTS

Figure 4 presents the global polarization of Λ and $\bar{\Lambda}$ as a function of the collision energy for the 20–50% centrality bin in Au+Au collisions. The results from this analysis are shown together with the results from lower collision energies $\sqrt{s_{NN}}$ = 7.7–62.4 GeV [14]. The 2007 result for $\sqrt{s_{NN}}$ = 200 GeV [13] has a large uncertainty and is consistent with zero. Our new results for $\sqrt{s_{NN}}$ = 200 GeV with significantly improved statistical precision reveal nonzero values of the polarization signal, $0.277 \pm 0.040\,(\text{stat}) \pm {}^{0.039}_{0.049}\,(\text{sys})$ [%] and $0.240 \pm 0.045\,(\text{stat}) \pm {}^{0.061}_{0.045}\,(\text{sys})$ [%] for Λ and $\bar{\Lambda}$, respectively, and are found to follow the overall trend of the collision energy dependence. While the energy dependence of the global polarization was not obvious from the lower energy results, together with the new 200 GeV results, the polarization is found to decrease at higher collision energy. Calculations for primary Λ and all Λ taking into account the effect of feed-down from a 3+1D viscous hydrodynamic model vHLLE with the UrQMD initial state [15] are shown for comparison. The model calculations agree with the data over a wide range of collision energies, including $\sqrt{s_{NN}}$ = 200 GeV within the current accuracy of our experimental measurements. Calculations from a Multi-Phase Transport (AMPT) model predict slightly higher polarization than the hydrodynamic model but are also in good agreement with the data within uncertainties. Neither of the models accounts for the effect of the magnetic field or predicts significant difference in Λ and $\bar{\Lambda}$ polarization due to any other effect, e.g., nonzero baryon chemical potential makes the polarization of particles lower than that of antiparticles, but the effect is expected to be small [40]. Other theoretical calculations [18,41] such as a chiral kinetic approach with the quark coalescence model [42] can also qualitatively reproduce the experimental data. It should be noted that most of the models calculate the spin polarization from the local vorticity at the freeze-out hypersurface. However, it is not clear when and how the vorticity and polarization are coupled during the system evolution and how much the hadronic rescattering at the later stage affects the spin polarization.

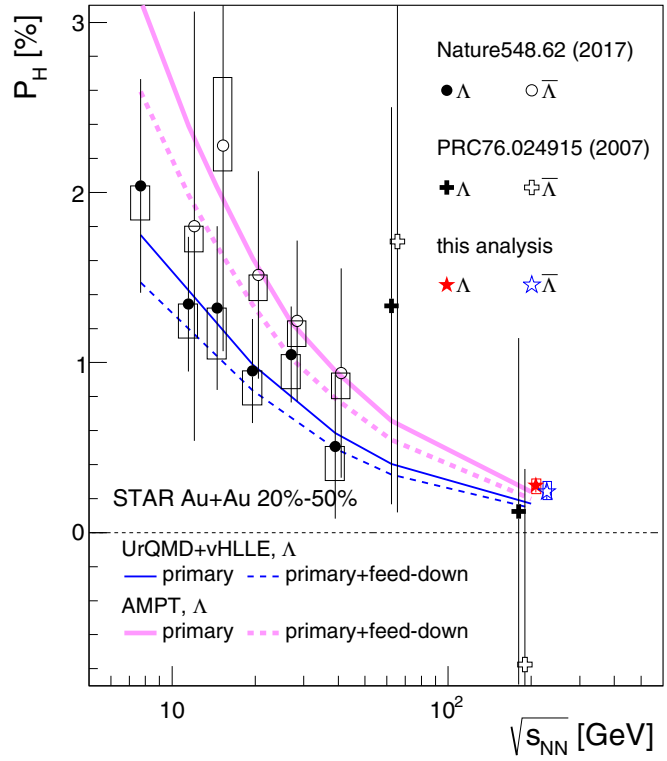

FIG. 4. Global polarization of Λ and $\bar{\Lambda}$ as a function of the collision energy $\sqrt{s_{NN}}$ for 20–50% centrality Au+Au collisions. Thin lines show calculations from a 3+1D cascade + viscous hydrodynamic model (UrQMD+vHLLE) [15] and bold lines show the AMPT model calculations [16]. In the case of each model, primary Λ with and without the feed-down effect are indicated by dashed and solid lines, respectively. Open boxes and vertical lines show systematic and statistical uncertainties, respectively. Note that the data points at 200 GeV and for $\bar{\Lambda}$ are slightly horizontally shifted for visibility.

We also performed differential measurements of the polarization versus the collision centrality, the hyperon's transverse momentum, and the hyperon's pseudorapidity. The vorticity of the system is expected to be smaller in more central collisions because of smaller initial source tilt [8,33] and/or because the number of spectator nucleons becomes smaller. Therefore, the initial longitudinal flow velocity, which would be a source of the initial angular momentum of the system, becomes less dependent on the transverse direction [12]. Figure 5 presents the centrality dependence of the polarization. The polarization of Λ and $\bar{\Lambda}$ is found to be larger in more peripheral collisions, as expected from an increase in the thermal vorticity [43]. With the given large uncertainties, it is not clear if the polarization saturates or even starts to drop off in the most peripheral collisions.

Figure 6 shows the polarization as a function of p_T for the 20–60% centrality bin. The polarization dependence on p_T is weak or absent, considering the large uncertainties, which is consistent with the expectation that the polarization is generated by a rotation of the system and therefore does not have

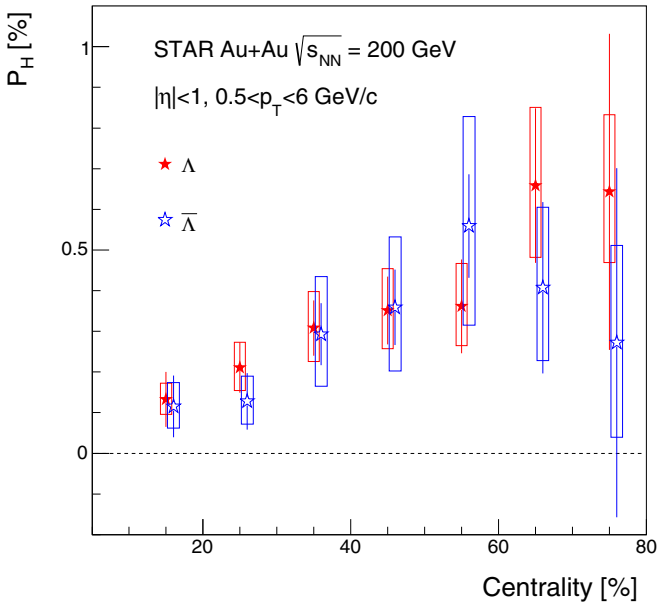

FIG. 5. Λ ($\bar{\Lambda}$) polarization as a function of the collision centrality in Au+Au collisions at $\sqrt{s_{NN}} = 200$ GeV. Open boxes and vertical lines show systematic and statistical uncertainties. The data points for $\bar{\Lambda}$ are slightly shifted for visibility.

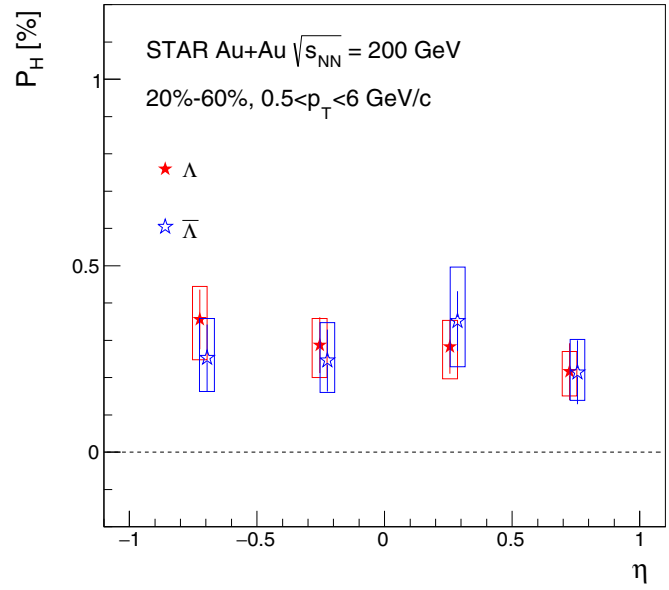

FIG. 7. Polarization of Λ and $\bar{\Lambda}$ as a function of η for the 20–60% centrality bin in Au+Au collisions at $\sqrt{s_{NN}} = 200$ GeV. Open boxes and vertical lines show systematic and statistical uncertainties. Note that the data points for $\bar{\Lambda}$ are slightly shifted for visibility.

a strong p_T dependence. One might expect a decrease of the polarization at lower p_T due to the smearing effect caused by scattering at the later stage of the collisions, and/or a decrease of polarization at higher p_T because of a larger contribution from jet fragmentation, but it is difficult to discuss such effects given the current experimental uncertainties. Calculations for primary Λ from a hydrodynamic model with two different initial conditions (ICs) [44] are compared to the data. The p_T dependence of the polarization slightly depends on the initial conditions, i.e., Glauber IC with the initial tilt of the source [8,9] and the initial state from the UrQMD model [45]. The UrQMD IC includes a preequilibrium phase which leads to the initial flow, but the Glauber IC does not include it, and the initial energy density profile is different between the two ICs, both of which would affect the initial angular momentum. The data are closer to the UrQMD IC but on average are slightly higher than the calculations.

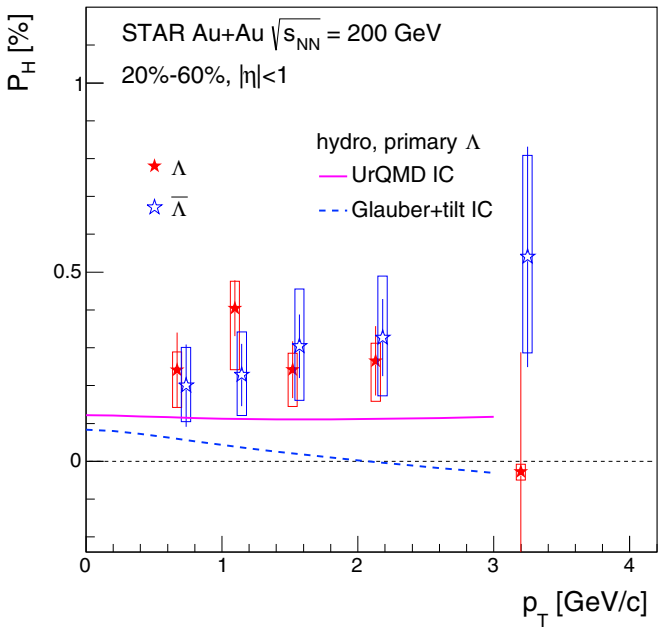

FIG. 6. Polarization of Λ and $\bar{\Lambda}$ as a function of p_T for the 20%–60% centrality bin in Au+Au collisions at $\sqrt{s_{NN}} = 200$ GeV. Open boxes and vertical lines show systematic and statistical uncertainties, respectively. Hydrodynamic model calculations for Λ with two different IC are compared. Note that the data points for $\bar{\Lambda}$ are slightly shifted for visibility.

Figure 7 presents the pseudorapidity dependence of the polarization for Λ and $\bar{\Lambda}$. It is consistent with being constant within uncertainties. The vorticity is expected to decrease at large rapidities but might also have a local minimum at $\eta = 0$ due to complex shear flow structure [15,43,46]. Due to baryon transparency at higher collision energy and the event-by-event fluctuations in the participant center-of-mass, such a dependence might be difficult to observe within the acceptance of the STAR detector.

As mentioned in the Introduction, the vorticity might be also related to anomalous chiral effects [19]. In addition to the contribution from the chiral vortical effect discussed in Ref. [18], the axial current $\mathbf{J}_5$ can be generated in the medium with nonzero vector chemical potential μ_v by the magnetic field $\mathbf{B}$ ($\mathbf{J}_5 \propto e\mu_v\mathbf{B}$) via the chiral separation effect [47]. Note that $\mathbf{J}_5$ points along the magnetic field in the case of $e\mu_v > 0$ (where e is the particle electric charge) but is opposite for $e\mu_v < 0$. Since the directions of the magnetic field and the initial angular momentum of the system are parallel, an additional contribution by $\mathbf{J}_5$ to the polarization might be observed, i.e.,

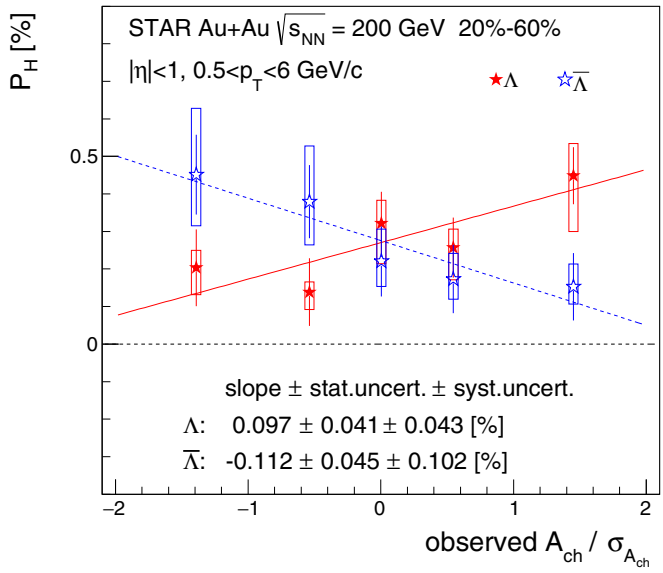

FIG. 8. Polarization of Λ and $\bar{\Lambda}$ as a function of observed charge asymmetry $A_{\rm ch}$ normalized with its RMS $\sigma_{A_{\rm ch}}$ for the 20–60% centrality bin in Au+Au collisions at $\sqrt{s_{NN}} = 200$ GeV. Open boxes and vertical lines show systematic and statistical uncertainties. Solid and dashed lines show linear fitting functions.

for $e\mu_v > 0$ ($e\mu_v < 0$), the spins of particles (antiparticles) in $\mathbf{J}_5$ are aligned to the direction of $\mathbf{B}$ which can contribute to the hyperon polarization. One can test this by studying the dependence of the polarization on the event charge asymmetry, $A_{\rm ch} = \langle N_+ - N_-\rangle/\langle N_+ + N_-\rangle$ where $N_{+(-)}$ denotes the number of positively (negatively) charged particles, assuming the relation $\mu_v/T \propto A_{\rm ch}$.

Figure 8 presents the polarization as a function of the event charge asymmetry $A_{\rm ch}$, where $A_{\rm ch}$ was normalized by its RMS, $\sigma_{A_{\rm ch}}$, to avoid a possible centrality bias, since the width of the $A_{\rm ch}$ distribution becomes wider in peripheral collisions. The results have large uncertainties, but the dependence on $A_{\rm ch}/\sigma_{A_{\rm ch}}$ seems to be different for Λ and $\bar{\Lambda}$. The data were fitted with a linear function and the extracted slope values are shown in Fig. 8. The observed difference in slopes is a 1–2σ effect. If confirmed by higher statistics measurements, this observation might open an important direction in studying chiral dynamics in heavy-ion collisions.

V. SUMMARY

We present the results of global polarization measurements for Λ and $\bar{\Lambda}$ hyperons in Au+Au collisions at $\sqrt{s_{NN}} =$ 200 GeV. With a 150-fold improvement in statistics compared to the previous measurements, we were able to measure the polarization with better than 1/10th of a percentage accuracy. Depending on centrality, a nonzero signal in the range of 0.1–0.5% was observed. We find no significant difference between Λ and $\bar{\Lambda}$ polarization at $\sqrt{s_{NN}} = 200$ GeV within the uncertainties. The present global polarization measurement at 200 GeV with its relatively small uncertainty adds significance to the earlier observed trend at lower RHIC energies [14] of the global polarization decrease with the collision energy. Within the uncertainties, our results agree with predictions from a hydrodynamic (UrQMD+vHLLE) and the AMPT models.

The polarization was also studied as functions of the collision centrality, the hyperon's transverse momentum, and the pseudorapidity. The polarization was found to be larger in more peripheral collisions, as expected from theoretical calculations, but no significant dependence on pseudorapidity or transverse momentum was observed. Furthermore, an indication of a polarization dependence on the event-by-event charge asymmetry was observed. This might be an indication of a possible contribution to the global polarization from the axial current induced by the initial magnetic field, although the statistical uncertainties need to be improved to reach a definitive conclusion.

ACKNOWLEDGMENTS

We thank the RHIC Operations Group and RCF at BNL, the NERSC Center at LBNL, and the Open Science Grid consortium for providing resources and support. This work was supported in part by the Office of Nuclear Physics within the U.S. DOE Office of Science; the U.S. National Science Foundation; the Ministry of Education and Science of the Russian Federation; National Natural Science Foundation of China; Chinese Academy of Science; the Ministry of Science and Technology of China and the Chinese Ministry of Education; the National Research Foundation of Korea; Czech Science Foundation and Ministry of Education, Youth and Sports of the Czech Republic; Department of Atomic Energy and Department of Science and Technology of the Government of India; the National Science Centre of Poland; the Ministry of Science, Education and Sports of the Republic of Croatia; RosAtom of Russia and German Bundesministerium fur Bildung, Wissenschaft, Forschung and Technologie (BMBF); and the Helmholtz Association.

[1] K. Yagi, T. Hatsuda, and Y. Miake, Quark-gluon plasma: From big bang to little bang, Camb. Monogr. Part. Phys. Nucl. Phys. Cosmol. **23**, 1 (2005).

[2] U. Heinz and R. Snellings, Collective flow and viscosity in relativistic heavy-ion collisions, Ann. Rev. Nucl. Part. Sci. **63**, 123 (2013).

[3] S. A. Voloshin, A. M. Poskanzer, and R. Snellings, Collective phenomena in non-central nuclear collisions, in *Relativistic Heavy Ion Physics*, edited by R. Stock, Landolt-Börnstein - Group I Elementary Particles, Nuclei and Atoms, Vol. 23 (Springer-Verlag, Berlin, Heidelberg, 2010), p. 293.

[4] C. Gale, S. Jeon, B. Schenke, P. Tribedy, and R. Venugopalan, Event-by-Event Anisotropic Flow in Heavy-Ion Collisions from Combined Tang-Mills and Viscous Fluid Dynamics, Phys. Rev. Lett. **110**, 012302 (2013).

[5] L. P. Csernai and D. Röhrich, Third flow component as QGP signal, Phys. Lett. B **458**, 454 (1999).

[6] J. Brachmann, S. Soff, A. Dumitru, H. Stöcker, J. A. Maruhn, W. Greiner, L. V. Bravina, and D. H. Rischke, Antiflow of nucleons at the softest point of the EoS, Phys. Rev. C **61**, 024909 (2000).

[7] L. Adamczyk *et al.* (STAR Collaboration), Beam-Energy Dependence of the Directed Flow of Protons, Antiprotons, and Pions in Au+Au Collisions, Phys. Rev. Lett. **112**, 162301 (2014).

[8] P. Bożek and I. Wyskiel, Directed flow in ultrarelativistic heavy-ion collisions, Phys. Rev. C **81**, 054902 (2010).

[9] F. Becattini, G. Inghirami, V. Rolando, A. Beraudo, L. Del Zanna, A. De Pace, M. Nardi, G. Pagliara, and V. Chandra, A study of vorticity formation in high energy nuclear collisions, Eur. Phys. J. C **75**, 406 (2015).

[10] Z. T. Liang and X. N. Wang, Globally Polarized Quark-Gluon Plasma in Noncentral A+A Collisions, Phys. Rev. Lett. **94**, 102301 (2005); **96**, 039901(E) (2006).

[11] S. A. Voloshin, Polarized secondary particles in unpolarized high energy hadron-hadron collisions? arXiv:nucl-th/0410089 [nucl-th].

[12] F. Becattini, F. Piccinini, and J. Rizzo, Angular momentum conservation in heavy ion collisions at very high energy, Phys. Rev. C **77**, 024906 (2008).

[13] B. I. Abelev *et al.* (STAR Collaboration), Global polarization measurement in Au+Au collisions, Phys. Rev. C **76**, 024915 (2007); **95**, 039906(E) (2017).

[14] L. Adamczyk *et al.* (STAR Collaboration), Global Λ hyperon polarization in nuclear collisions, Nature **548**, 62 (2017).

[15] I. Karpenko and F. Becattini, Study of Λ polarization in relativistic nuclear collisions at $\sqrt{s_{NN}} = 7.7$–200 GeV, Eur. Phys. J. C **77**, 213 (2017).

[16] H. Li, L.-G. Pang, Q. Wang, and X.-L. Xia, Global Λ polarization in heavy-ion collisions from a transport model, Phys. Rev. C **96**, 054908 (2017).

[17] M. A. Lisa *et al.* (E895 Collaboration), Azimuthal dependence of pion interferometry at the AGS, Phys. Lett. B **496**, 1 (2000).

[18] M. Baznat, K. Gudima, A. Sorin, and O. Teryaev, Hyperon polarization in Heavy-Ion Collisions and gravity-related anomaly, Phys. Rev. C **97**, 041902 (2018).

[19] D. E. Kharzeev, J. Liao, S. A. Voloshin, and G. Wang, Chiral magnetic and vortical effects in high-energy nuclear collisions—A status report, Prog. Part. Nucl. Phys. **88**, 1 (2016).

[20] F. Becattini, I. Karpenko, M. A. Lisa, I. Upsal, and S. A. Voloshin, Global hyperon polarization at local thermodynamic equilibrium with vorticity, magnetic field and feed-down, Phys. Rev. C **95**, 054902 (2017).

[21] S. A. Voloshin,Vorticity and particle polarization in heavy ion collisions (experimental perspective), in *Proceedings of the 17th International Conference on Strangeness in Quark Matter (SQM 2017)* [EPJ Web Conf. **171**, 07002 (2018)].

[22] K. H. Ackermann *et al.* (STAR Collaboration), STAR detector overview, Nucl. Instrum. Methods A **499**, 624 (2003).

[23] M. Anderson *et al.*, The STAR time projection chamber: A unique tool for studying high multiplicity events at RHIC, Nucl. Instrum. Methods A **499**, 659 (2003).

[24] W. J. Llope (STAR Collaboration), Multigap RPCs in the STAR experiment at RHIC, Nucl. Instrum. Methods A **661**, S110 (2012).

[25] W. J. Llope *et al.* (STAR Collaboration), The STAR Vertex Position Detector, Nucl. Instrum. Methods A **759**, 23 (2014).

[26] C. Adler, A. Denisov, E. Garcia, M. Murray, H. Strobele, and S. White, The RHIC zero degree calorimeters, Nucl. Instrum. Methods A **461**, 337 (2001).

[27] J. Schambach *et al.*, The STAR Heavy Flavor Tracker (HFT), in *Proceedings of the 20th International Conference on Particles and Nuclei (PANIC '14)* (2014), p. 659.

[28] G. Contin *et al.*, The STAR Heavy Flavor Tracker (HFT): Focus on the MAPS based PXL detector, Nucl. Part. Phys. Proc. **273**, 1155 (2016).

[29] L. Adamczyk *et al.* (STAR Collaboration), Inclusive charged hadron elliptic flow in Au+Au collisions at $\sqrt{s_{NN}} = 7.7$–39 GeV, Phys. Rev. C **86**, 054908 (2012).

[30] J. Adams *et al.* (STAR Collaboration), Directed flow in Au+Au collisions at $\sqrt{s_{NN}} = 62.4$ GeV, Phys. Rev. C **73**, 034903 (2006).

[31] B. I. Abelev *et al.* (STAR Collaboration), System-Size Independence of Directed Flow Measured at the BNL Relativistic Heavy Ion Collider, Phys. Rev. Lett. **101**, 252301 (2008).

[32] S. A. Voloshin and T. Niida, Ultra-relativistic nuclear collisions: Direction of spectator flow, Phys. Rev. C **94**, 021901(R) (2016).

[33] L. Adamczyk *et al.* (STAR Collaboration), Azimuthal anisotropy in Cu+Au collisions at $\sqrt{s_{NN}} = 200$ GeV, arXiv:1712.01332 [Phys. Rev. C (to be published)].

[34] A. M. Poskanzer and S. A. Voloshin, Methods for analyzing anisotropic flow in relativistic nuclear collisions, Phys. Rev. C **58**, 1671 (1998).

[35] C. Patrignani *et al.* (Particle Data Group), Review of particle physics, Chin. Phys. C **40**, 100001 (2016).

[36] L. Adamczyk *et al.* (STAR Collaboration), Elliptic flow of identified hadrons in Au+Au collisions at $\sqrt{s_{NN}} = 7.7$–62.4 GeV, Phys. Rev. C **88**, 014902 (2013).

[37] N. Borghini and J. Y. Ollitrault, Azimuthally sensitive correlations in nucleus-nucleus collisions, Phys. Rev. C **70**, 064905 (2004).

[38] B. I. Abelev *et al.* (STAR Collaboration), Spin alignment measurements of the $K^{*0}(892)$ and $\phi(1020)$ vector mesons in heavy ion collisions at $\sqrt{s_{NN}} = 200$ GeV, Phys. Rev. C **77**, 061902(R) (2008).

[39] N. Borghini, P. M. Dinh, and J. Y. Ollitrault, Analysis of directed flow from elliptic flow, Phys. Rev. C **66**, 014905 (2002).

[40] R.-H. Fang, L.-G. Pang, Q. Wang, and X.-N. Wang, Polarization of massive fermions in a vortical fluid, Phys. Rev. C **94**, 024904 (2016).

[41] Y. Xie, D. Wang, and L. P. Csernai, Global Λ polarization in high energy collisions, Phys. Rev. C **95**, 031901 (2017).

[42] Y. Sun and C. M. Ko, Λ hyperon polarization in relativistic heavy ion collisions from a chiral kinetic approach, Phys. Rev. C **96**, 024906 (2017).

[43] Y. Jiang, Z.-W. Lin, and J. Liao, Rotating quark-gluon plasma in relativistic heavy ion collisions, Phys. Rev. C **94**, 044910 (2016); **95**, 049904(E) (2017).

[44] F. Becattini and Iu. Karpenko, Collevtive Longitudinal Polarization in Relativistic Heavy-Ion Collisions at Very High Energy, Phys. Rev. Lett. **120**, 012302 (2018).

[45] I. A. Karpenko, P. Huovinen, H. Petersen, and M. Bleicher, Estimation of the shear viscosity at finite net-baryon density from $A + A$ collision data at $\sqrt{s_{\rm NN}} = 7.7-200$ GeV, Phys. Rev. C **91**, 064901 (2015).

[46] W.-T. Deng and X.-G. Huang, Vorticity in heavy-ion collisions, Phys. Rev. C **93**, 064907 (2016).

[47] S. Schlichting (private communication, 2017).